IET Renewable Power Generation

WILEY

The Institution of Engineering and Technology

ORIGINAL RESEARCH OPEN ACCESS

Assessment of Post-Fault Voltage Recovery in IBRs-Dominated Grids: Evaluating the Role of Grid-Forming Converters

Rafat Aljarrah[1] | Qusay Salem[1] | Mazaher Karimi[2] | Ibrahim Abuishmais[1] | Hamza Jaber[1]

[1]Electrical Engineering Department, Princess Sumaya University for Technology, Amman, Jordan | [2]School of Technology and Innovations, University of Vaasa, Vaasa, Finland

Correspondence: Mazaher Karimi (mazaher.karimi@uwasa.fi)

Received: 16 October 2025 | **Revised:** 24 March 2026 | **Accepted:** 3 July 2026

ABSTRACT

Conventional Synchronous Generators (SGs) are increasingly being replaced by Inverter-Based Resources (IBRs) for integrating Renewable Energy Sources (RESs). However, this transition introduces significant challenges, as most existing IBRs employ Grid-Following (GFL) converters that depend on a strong grid connection for stable operation. Consequently, their ability to provide dynamic voltage support and maintain post-fault voltage recovery might be limited in IBR-dominated grids. To address these issues, grid-forming (GFM) converters have emerged as a promising alternative. Unlike GFL converters, GFM units can emulate SG behaviour by autonomously establishing grid voltage and frequency, thereby enhancing both steady-state performance and dynamic response during disturbances. This study investigates the potential role that GFM converters may play in improving dynamic voltage support and post-fault voltage recovery in IBR-dominated grids. It first examines post-fault voltage recovery in conventional SG-based systems, then evaluates various IBR penetration scenarios, with low, medium, and high penetrations of IBRs based on both traditional GFL and emerging GFM converters, integrated to replace large and central SGs. Finally, a correlation-based sensitivity analysis is introduced to systematically quantify the relationship between fault-induced voltage nadir and voltage recovery speed across network locations and penetration levels of IBRs. Through simulations and analysis using a modified IEEE 9-bus test system modelled in DIgSILENT PowerFactory, the study demonstrates the vital role of GFM converters in ensuring robust post-fault voltage response and overall grid stability in renewable-rich power systems.

1 | Introduction

To manage voltage levels, the severity of the disturbance, voltage dip propagation through the system, and post-fault voltage performance, Synchronous Generators (SGs) have traditionally provided dynamic support during system disturbances such as short-circuit (SC) faults [1–3]. To an extent, dynamic voltage support has been ensured in conventional SG-based systems with adequate system strength and high fault levels, also referred to as short-circuit MVA, provided by SGs. However, the high penetration of inverter-based resources (IBRs) has become a notable feature of modern power systems, driven by the increasing share of renewable energy. Although IBRs facilitate the integration of clean energy into the power grids, their extensive penetration levels come with challenges [3, 4]. This is not only because such integration has been accompanied by increased displacement of large SGs, but also because grid-following (GFL) converters synchronise with the grid voltage and frequency. Although GFL converters are required to ride through the faults and to adapt their controllers to provide the necessary dynamic voltage support, their capability to do so and to function effectively might be limited as they rely on a strong system connection, where the presence of SGs is essential [5]. Moreover, the level of the support provided through reactive power is much less than that traditionally offered by SGs, as they act as a current source [6]. Since the systems are moving towards extensive penetrations of IBRs, even to 100%, their capability to provide such functionality and to support might be challenging, especially after severe grid disturbances [3]. In addition, the capability of GFL converters to comply with grid codes and meet the proper fault-ride-through (FRT) requirements is in question. This, in turn, will pose a significant obstacle to dynamic voltage support and post-fault voltage response in IBRs-dominated grids. The aforementioned limitations of such IBRs utilising GFL converters make it harder to ensure such requirements [3]. On the other hand, new technology based on grid-forming (GFM) converters has been proposed as a potential alternative to bridge this gap [7–9]. Such converters would be expected to provide functionality to form the grid voltage and frequency, meaning they have the potential to rely less on grid stiffness and to contribute to greater IBR penetration.

A lot of research has raised the issues and challenges associated with the increased penetration of GFL-based IBRs. Some of them have pointed to the difficulties that may be faced by the traditional IBRs employing GFL converters [3, 10, 11]. Another category has focused on the grid impact when operating with IBR-dominated scenarios, including stability, system strength, and protection challenges [12–15]. While some studies have proposed enhancements that may improve the performance of such GFL converters, they have highlighted the need for more robust technology.

Recent literature has examined the advancement of the newly proposed GFM converters and the roles they may play in future power systems [3, 6–9, 16, 17]. While a decent number have discussed the concept of the GFM technology with different control schemes [17]. Another category of research has focused on the main differences between GFM and GFL converters, outlining the advantageous properties and the additional capabilities that GFM converters may provide [18, 19]. Another area of research can be found about the performance of GFM converters concerning the stability of such converters under different operating conditions [20, 21]. For instance, the work in [20] has proposed a novel power model for parallel operation of GFM converters and investigated the steady-state angle stability. The work in [21] has presented a novel model-orientated strategy to improve the transient stability of GFM and the transient post-fault behaviour. However, very little research has been conducted to investigate the actual impact of such GFM technology on grid performance in IBRs-dominated networks, especially from the perspectives of dynamic voltage support and post-fault response.

Researchers in [22] have highlighted the importance of introducing GFM converters to provide adequate voltage support while considering and enhancing grid strength through small-signal analysis. They have concluded that such GFM incorporates an advantage rather than modified GFL. However, large-signal stability and dynamic voltage support during severe grid disturbances have not been considered. The study in [23] shows that integrating GFM converters with battery energy storage systems can significantly improve microgrid stability by enabling effective fault ride-through and rapid recovery during grid disturbances. However, the study was conducted at the microgrid level, without accounting for different penetration levels of IBRs. In [4], the impact of the GFM converters on the voltage dip propagation during severe disturbances has been investigated. The work concludes that incorporating GFM converters enhances voltage stability compared to GFL converters by reducing voltage dips and distortion during faults. However, post-fault voltage recovery might be more sensitive to the penetration level of GFM converters.

Although the aforementioned studies have provided a strong insight into different aspects accounting for GFM converters' control, stability, and superior behaviour when compared to GFL converters, they have not fully covered the grid impact and the efficacy of the proposed GFM converters on the dynamic voltage support and the post-fault voltage response in scenarios of high penetration of IBRs. This necessitates further investigation of these aspects to understand better the need, the shortages, and the potential role of GFM converters in such scenarios. Accordingly, this paper addresses this gap by providing a systematic analysis of the role of GFM converters in enhancing dynamic voltage support during severe SC faults and by quantitatively assessing the sensitivity of post-fault voltage recovery to different penetration levels of IBRs, distinguishing between GFL and GFM technologies.

The rest of the paper is organised as follows: Section 2 presents an overview of GFL and GFM-based IBRs and introduces the concept of droop-based GFM converters, covering modelling, control, and current limiting during grid disturbances. Section 3 presents the research methodology. Section 4 presents and discusses the results and findings. And finally, Section 5 concludes the paper.

2 | Grid-Following (GFL) versus Grid-Forming (GFM) IBRs

Traditional GFL converters have been used extensively for integrating RESs. While they provide a synchronised interface for such RESs, they rely on grid voltage and frequency, and they generally follow the grid voltage for their current injection. Hence, any change in the grid voltage will be followed by a change in the converter voltage to keep providing the required power. In other words, maintaining the power set point requires the converter to adjust its voltage, mimicking the behaviour of a controlled current source. On the other hand, GFM converters are designed to form the grid voltage by accommodating their current injection. This behaviour mimics the SGs; hence, they can be modelled as a voltage source in series with an impedance [24]. Figure 1 shows the simplified models of GFL and GFM converters, while Figure 2 shows the phasor diagrams of both IBRs in response to a change in the grid voltage [25]. Note that I and E represent the current source of the GFL converter and the internal voltage source of the GFM converter, respectively. Z_c denotes the converter output impedance, Z_g is the grid impedance, I_c is the converter output current, V_c is the point-of-common-coupling voltage, and V_g represents the grid voltage. The phasor diagrams illustrate the basic distinction between GFM and GFL converters' instantaneous responses to grid voltage fluctuations. Observe that the GFL converter acts as a controlled current source that keeps the injected current phasor I_g initially constant, any change in the grid voltage V_g causes the converter terminal voltage to adjust

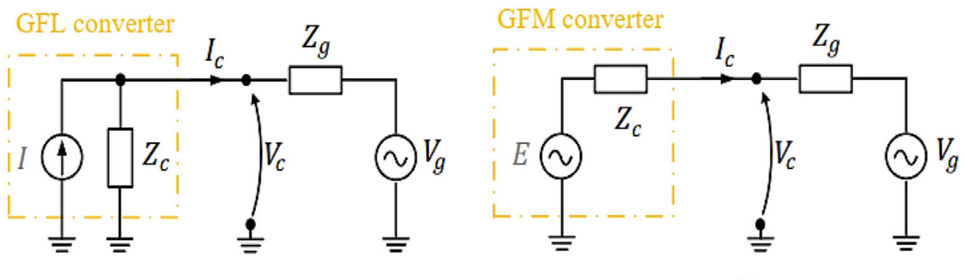

FIGURE 1 | Simplified models of IBRs: (a) GFL, (b) GFM [25].

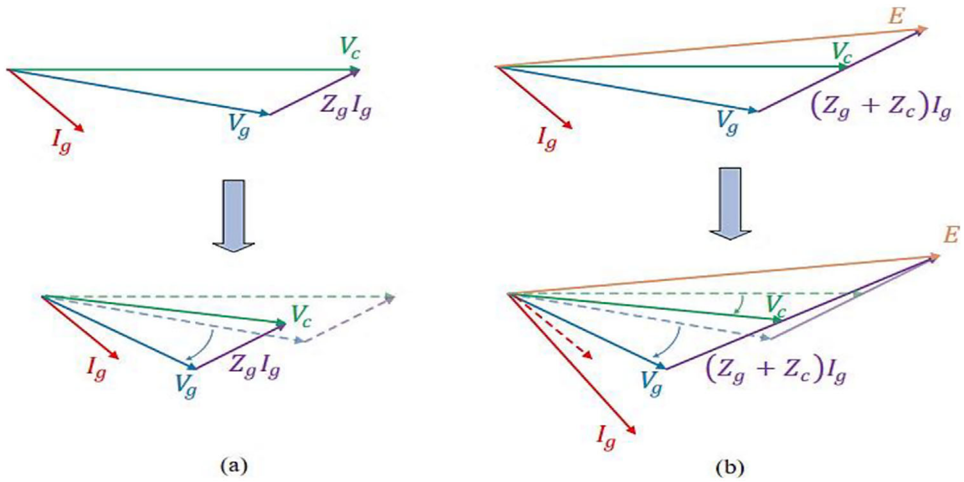

FIGURE 2 | The phasor diagram of IBRs in response to a grid voltage change: (a) GFL (b) GFM [25].

accordingly. In contrast, the GFM converter which functions as a voltage source behind an impedance, causing an instantaneous shift in the current I_g because the internal voltage E is initially unaffected by the disturbance.

GFM and GFL converters are almost identical in structure. For instance, both technologies are categorised as voltage-source converters, with main components similar to the primary energy source, the DC link, the switching converter, the control board, and the output filter. However, the fundamental differences lie in the control strategy and the synchronising mechanism [9]. In GFL converters, an explicit synchronisation element, such as a phase-locked loop (PLL), receives the measured voltage and determines its phase angle and frequency to synchronise the converter with the grid [26]. This phase angle then feeds other control blocks, and the power exchange will be determined accordingly. On the other hand, the GFM converters generate their own voltage and frequency references, independent of the grid, and control their output voltage and frequency to align with the grid without using a PLL; hence, they can be operated as a standalone system when needed. In the literature, several control strategies have been proposed to synchronise the GFM and enable its functionality. This includes mainly two categories: droop-based GFM and synchronous machine-based GFM [27, 28]. Droop-based GFM control has been widely adopted in the literature and is considered the most common control type for GFM converters. Under the umbrella of droop-based control of GFM, different types can be found, such as frequency-based droop, angle-based

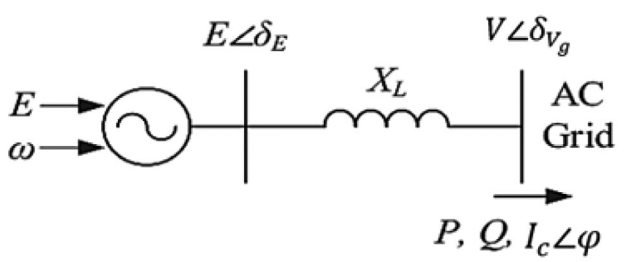

FIGURE 3 | Basic model of GFM converter [28].

droop, and Power Synchronisation Control (PSC) [28]. Droop-based GFM control has proven its simplicity, high reliability, independence from communication [28], well-developed droop control based on power decoupling characteristics [29], and the capability to improve grid strength and stability [30]. Therefore, in this paper, the droop-based GFM converter is adopted for comparison with GFL converters in terms of dynamic voltage support and post-fault voltage response enhancement in power systems with high IBR penetration. Acting as a voltage source, the droop-based GFM converter can be modelled as a voltage source behind the coupling reactance, where the voltage and the angular frequency are controlled by the internal converter control, as shown in Figure 3 [29]. According to [29, 31], when properly selected, the converter impedance Z_c, which is represented by the coupling reactance, X_L, can play a key role in decoupling the active and reactive power of the converter. Doing so, will result

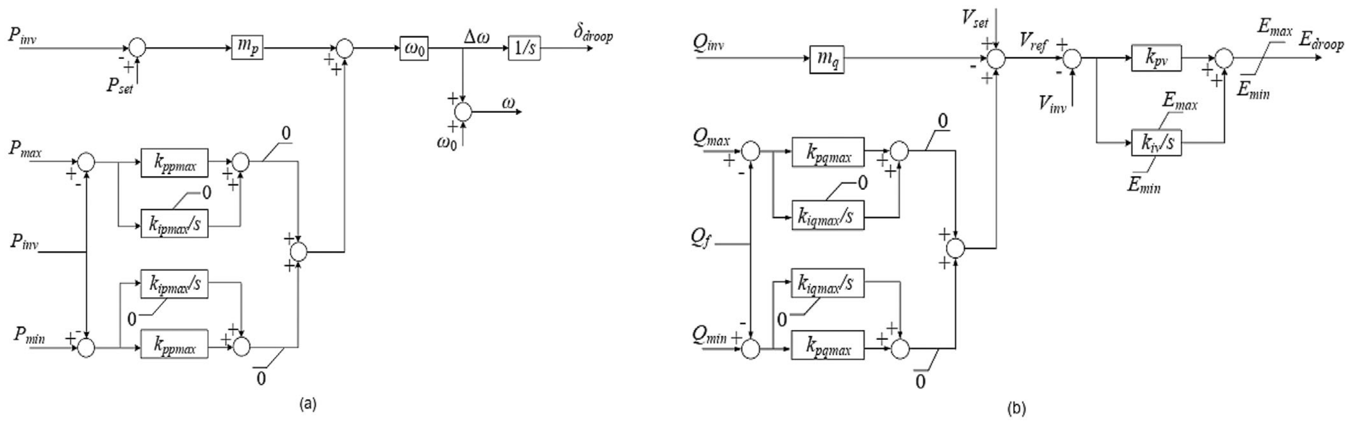

FIGURE 4 | Droop control: (a) P/F droop control and overload mitigation control and (b) Q/V droop control [29].

in a linear relationship between both the active power P, and the phase angle difference δ_P. both the same is applied for both reactive power Q and the voltage E. Equations (1), (2), and (3) represents this decoupling characteristic.

$$\delta_P = \delta_E - \delta_{V_g} \tag{1}$$

$$P = \frac{EV_g}{X_L} \sin \delta_P \approx P = \frac{EV_g}{X_L} \delta_P \tag{2}$$

$$Q = \frac{E^2 - EV_g \cos \delta_P}{X_L} \approx \frac{E\left(E - V_g\right)}{X_L} \tag{3}$$

Figure 4, shows both P/F and Q/V droop controls and how they provide both E_{droop} and δ_{droop} to control the behaviour of the converter. It is worth noting that by adjusting the angular frequency to avoid excessive power output following disturbances, the P/F droop control can synchronise the phase angles of many GFM converters, ensuring synchronisation throughout parallel operation when it exists. Also, by regulating E_{droop} and maintaining a predetermined voltage characteristic, the Q/V droop ensures that reactive power output remains within predetermined bounds ($Q_{\max}$ and $Q_{\min}$). More details on the definition, full description, and values of the discussed parameters can be found in [29].

According to the described control, the droop-based GFM converter would react to grid disturbances, such as SC faults, by adjusting its current to maintain voltage control. In shallow voltage dip cases, the current might stay within the converter's switching capability. Still, in severe voltage dip cases, it might exceed the limits, causing damage to the power electronic switches. Hence, such GFM converters must be equipped with a current-limiting mechanism that allows them to ride through the fault safely. To achieve this, the droop control continuously monitors the current until a disturbance, represented by a current exceeding the maximum limit, is observed. In normal operation conditions and during shallow faults seen by the converter, where the current is within the maximum limit, the voltage of the converter is determined by the droop control, and the current is calculated using Equation (4). However, once the current limit is violated, the converter voltage is determined by the grid voltage and the voltage drop through the coupling reactance using Equation (5), and the converter current is calculated accordingly.

$$I_c\angle\varphi = \frac{E_{droop}\angle\delta_{droop} - V\angle\delta_{V_g}}{jX_L} \tag{4}$$

$$E\angle\,\delta_E = V_g\,\angle\delta_{V_g} + jX_L I_{max}\angle\varphi \tag{5}$$

It is worth noting that such a current-limiting mechanism allows the GFM converter to limit the fault current without changing the pre-fault phase angle of the current. This is unlike the case of GFL converters, where the current and the angle would be changed according to a predefined *k*-factor (proportional gain) that prioritises the reactive current injection during the fault [32]. Moreover, the GFM control may allow faster fault current injection (e.g., within 5 ms [33]) due to its unchanged control compared to the GFL one, where a delay might be observed (e.g., 20 ms or more [34]). These differences, in addition to the pre- and post-fault differences in control functionality, might not only lead to different dynamic voltage support during grid faults but also to a distinct impact on the post-fault voltage response of the system behaviour, especially in scenarios of high penetration of IBRs, which will be thoroughly investigated in the following sections. It is worth noting that different current-limiting mechanisms have been proposed in the literature, which may lead to different transient responses when considered. However, a comprehensive comparative assessment of these methods is beyond the scope of this paper. More details on such proposed current-limiting strategies can be found in [33, 35, 36].

It is worth noting that developing detailed converter models from first principles is beyond the scope of this study. Instead, validated generic models available in DIgSILENT PowerFactory are employed, as they adequately capture the dominant dynamics governing post-fault voltage recovery. GFL scenarios are represented using the built-in Type-IV wind template, while a generic droop-controlled template for a GFM converter, which is modelled using what is described in Section 2, has been utilised. Note that a current limit of 1.2 p.u. for both cases is considered. This approach ensures a fair comparison while maintaining simplicity and enabling straightforward reproducibility by other researchers.

3 | Methodology

The methodology of this research is aimed at examining post-fault voltage performance when different penetrations of IBRs (both GFL and GFM) occur. The voltage behaviour of the system after exposure to severe three-phase bolted faults is examined by evaluating dynamic voltage support during the fault and voltage recovery after fault clearing. At first, a traditional power grid based solely on conventional SGs is studied as a base case. Then, the system is modified by installing IBRs at different penetrations of GFL and GFM technologies, partially replacing the SGs in the system, to evaluate the effects of several IBR penetration scenarios. The scenarios of interest in this study cover a wide range of IBRs penetrations, enabling a holistic assessment of IBRs' impact on voltage performance. While considering both GFM and GFL simultaneously is a relevant scenario, it is beyond the scope of the current work. Note that the evaluation is not conducted solely by monitoring voltage waveforms during and after the fault; it also relies on several metrics extracted and compared across all scenarios. This includes:

- The pre-fault voltage, $V_{\text{pre-fault}}$: the steady-state voltage level before the fault starts.
- The voltage nadir, V_{nadir}: the minimum voltage during the fault.
- The steady-state voltage, V_{ss}: the steady voltage reached after clearing the fault.
- Voltage deviation, ΔV: Absolute voltage difference between $V_{\text{pre-fault}}$ and V_{ss}.
- Overshoot percentage, OS%: the magnitude of the maximum overshoot observed after clearing the fault in per cent relative to the pre-fault voltage.
- The time of voltage nadir, t_{nadir}: the time instant at which the voltage nadir is observed in s.
- The time of 0.9 p.u voltage recovery, $t_{0.9}$: the time instant at which the voltage recovers to 0.9 p.u in s.
- The time of steady-state voltage, t_{ss}: the time at which the voltage reaches a new steady-state value with tolerance ± 2.

The findings of this study have been validated using the modified IEEE 9-BUS test system utilising the generic models for GFL and GFM converters available in DIgSILENT PowerFactory, which have been employed to create the modelled scenarios of different penetrations of IBRs-based RESs (represented by type-4 wind farms in this study). It is also worth noting that the GFM technology employed is based solely on droop-based control, while other GFM controls are beyond the scope of this research. Figure 5 shows the modified IEEE 9-bus test system with the scenarios modelled for this study. The scenarios for IBRs penetration are defined in Table 1.

Note that the penetration metric used here is the ratio of the installed IBRs' capacity to the total capacity of the generation units in the system. The mathematical expression of the penetration level ($p\%$) in percentage is expressed as follows:

$$p\% = \frac{\text{IBRs Capcity (MVA)}}{\text{Total Generation Capacity (MVA)}} \times 100 \qquad (6)$$

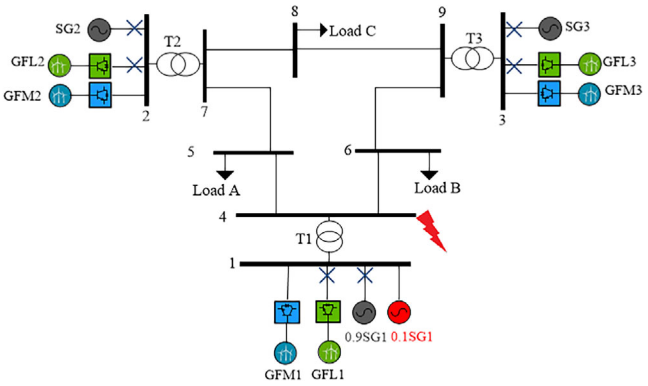

FIGURE 5 | The modified IEEE 9-bus test system at 96% GFM scenario.

TABLE 1 | The scenarios of IBRs' penetrations.

No.	Scenario name	IBR	IBR type	Replaced SGs
1	Base	0	None	None
2	22% GFL	22	GFL	SG-2
3	22%GFM	22	GFM	SG-2
4	33% GFL	33	GFL	SG-3
5	33% GFM	33	GFM	SG-3
6	55% GFL	55	GFL	SG-2 and SG-3
7	55% GFM	55	GFM	SG-2 and SG-3
8	96% GFL	96	GFL	SG-2, SG-3, 90% SG-1
9	96% GFM	96	GFM	SG-2, SG-3, 90% SG-1

4 | Results and Discussions

This section provides a thorough analysis of the post-fault voltage performance and how it may be affected by the voltage response during severe faults. First, the base scenario is considered, and a three-phase bolted fault is initiated at Bus 4, which is selected because it represents the strongest bus in the network before considering IBRs, with the highest short-circuit capacity and the lowest equivalent impedance. We have calculated the fault level (SC capacity MVA) in the base scenario and ranked the buses accordingly. Hence, selecting bus 4 allows the evaluation of system performance under severe fault conditions. The voltage during the fault period (0.1-0.25 s) and voltage recovery after clearing the fault have been studied and analysed. Then, the other penetration scenarios were created and simulated under the same faulty conditions to evaluate the impact of IBR penetration (both GFL and GFM) on voltage performance.

After that, the study is extended to examine the performance of the generation buses (namely, buses 1, 2, and 3) and the load buses (namely, buses 5, 6, and 8). This has been done considering all the aforementioned scenarios to allow examining the impact not only on the post-fault voltage performance at the faulty bus but also to allow extracting conclusions on the effect of such scenarios on the voltage recovery on buses of different strength, including generation locations, as they are the strongest, and the load centres, as they are the weakest, in

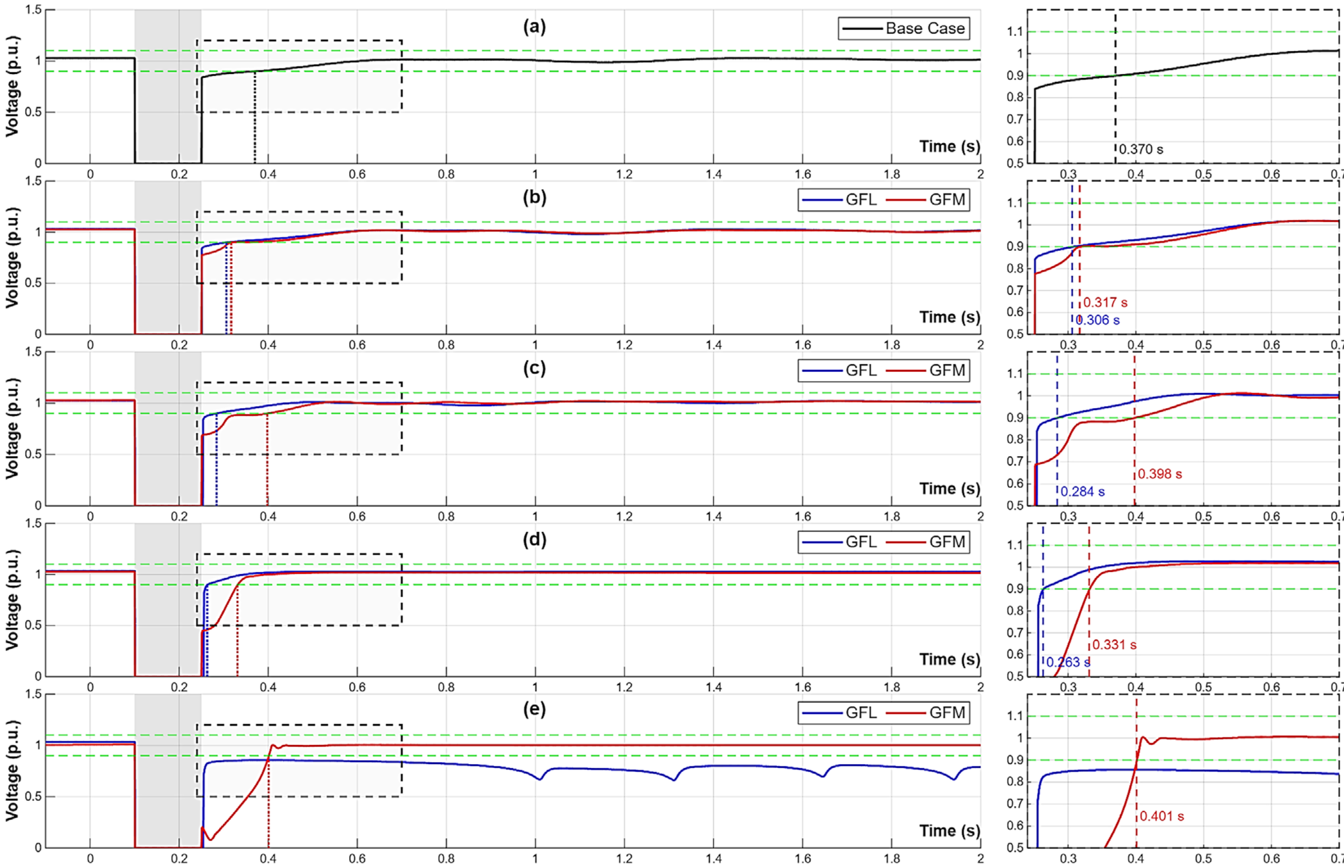

FIGURE 6 | Voltage response at Bus 4 at different penetration scenarios of IBRs: (a) Base case (zero%), (b) 22% IBRs, (c) 33% IBRs, (d) 55% IBRs, and (e) 96% IBRs.

the network. All voltage waveforms, along with the numerical metrics described earlier, have been extracted and compared from the IBR-based technology (GFL or GFM) perspective relative to the base scenario, where the system is run based on SGs only.

4.1 | Results at the Faulty Bus

The results of bus-4, where a bolted three-phase SC fault occurs for 150 ms, at different penetrations of GFL and GFM IBR technologies, have been monitored for 5 s. Still, the very short time after clearing the fault is highlighted and recorded within a 2s time window, as the waveforms are already in the steady-state condition. Observe Figure 6, which shows the results of the voltage waveform at bus 4 for a period of 2 s. Note that the immediate post-fault area is zoomed in near each subplot to allow better observation of the performance of the transition from faulty to voltage recovery conditions. The zoomed-in areas of each penetration level are presented on the right side of each subplot as shown in Figure 6. Note that in all scenarios, the voltage during fault reached zero due to the severity of the bolted SC fault (i.e., zero fault impedance).

4.1.1 | Base Scenario (*p* = 0%)

The resulting voltage waveform in the base scenario (e.g., zero % IBRs) has recovered to its 0.9 p.u value at around 0.37 s (i.e., $t_{0.9}$ = 0.37 s), which a relatively fast recovery. Note also that the voltage has reached a new steady-state value (V_{ss} = 1.012 p.u) compared to the value of pre-fault voltage, $V_{\text{pre-fault,}}$ of 1.026 p.u, registering a minimal deviation of 0.014 p.u., Observe that the voltage enters a steady-state period at t_{ss} = 0.58 s, with almost negligible overshoot (OS = 1.6%). Therefore, when combining the waveform performance and considering all these metrics, it can be concluded that bus-4 exhibits robust voltage recovery after a severe SC fault when considering the zero% penetration scenario, with quick restoration, little overshoot, and minimal steady-state deviation as shown in Figure 6a. Note that all the numerical metrics extracted from the voltage response during and after the fault for all scenarios are listed in Table 2.

4.1.2 | Low and Medium Scenarios (0% < *p* ≤ 55%)

For the low and medium penetration scenarios (e.g., up to 55%), the results show that both GFL and GFM would contribute to rapid recovery and low OS% (<2%), indicating stable, well-damped voltage recovery. Observe that both $t_{0.9}$ and tss decrease with the increased penetration of IBRs, especially in the GFL scenarios. For instance, the $t_{0.9}$ has decreased from 0.373 s at zero% down to (0.264 s and 0.332 s) at the 55% GFL and 55% GFM scenarios, respectively. Hence, a faster recovery has been obtained at such scenarios, with the fastest $t_{0.9}$ observed in GFL scenarios compared to GFM ones. This shows that higher GFL penetration accelerates voltage recovery, which might indicate a

TABLE 2 | Metrics of the voltage performance at bus-4.

Penetration scenario	V_{pre} (p.u)	V_{ss} (p.u)	OS (%)	ΔV	$t_{0.9}$	t_{ss}
Zero%	1.026	1.012	1.677	0.014	0.373	0.580
22% GFL	1.030	1.013	1.532	0.017	0.308	0.545
22% GFM	1.026	1.007	1.603	0.020	0.318	0.549
33% GFL	1.025	1.012	0.965	0.013	0.285	0.429
33% GFM	1.026	1.007	1.376	0.020	0.399	0.495
55% GFL	1.036	1.028	0.551	0.008	0.264	0.361
55% GFM	1.026	1.012	0.784	0.015	0.332	0.380
96% GFL	1.036	0.782	9.484	0.254	NaN	0.891
96% GFM	1.007	0.989	1.680	0.018	0.402	0.407

higher converter ability to provide fast reactive support, although both GFL and GFM have the same overrating capability. On the other hand, although GFM cases have slightly longer $t_{0.9}$, but they have shown comparable t_{ss}, meaning that GFMs stabilise smoothly but slightly slower in early recovery. It is worth noting that ΔV remains small (i.e., < 0.02 p.u.) for all scenarios up to 55%, confirming the stable voltage recovery.

4.1.3 | High Penetration Scenario ($p = 96\%$)

In a high penetration scenario where most of the generation units are replaced with IBRs, the system represents a weak grid, as the system strength characterised by the fault level MVA and the inertia are significantly decreased. The results show that the voltage deteriorates drastically in the GFL scenario, as the voltage did not recover and a significant ΔV of 0.254 p.u. and OS of 9.48 % have been registered, as observed from Figure 6e, which shows both 96% GFL and 96% GFM scenarios. This indicates a severe fault-induced delayed voltage recovery; hence, voltage instability. In other words, the system fails to recover and to re-establish a new steady-state voltage in the case of GFL due to the lack of a firm voltage reference and reduced system strength. On the other hand, when GFM is considered instead of GFL, the system has shown excellent voltage recovery even at very high IBR penetration levels. Note that the voltage recovers with a small ΔV of 0.018 p.u. and OS of 1.68 %, which are almost the same as the base case scenario of zero penetration. Observe that regardless of some delayed t0.9 compared to base scenario, the voltage has reached steady-state faster, $t_{ss} = 0.407$ s, with 0.173 s earlier than the base scenario where, $t_{ss} = 0.580$ s. Collectively, the results of 96% GFM scenario have shown an excellent recovery, demonstrating the ability of GFM-based IBRs in contributing to a fast and stable post-fault voltage performance, especially in weak grids with high penetration of IBRs.

4.2 | Results at the Generation Buses

In order to examine the behaviour of the voltage at the generation buses considering different penetration scenarios of GFL and GFM IBRs, the voltage waveforms of the generation buses (namely, bus 1, bus 2, and bus 3) have been obtained considering the previous severe SC fault at bus4. Note that all voltage waveforms and all metrics are obtained in the same way as in the previous sub-section (5.1), in addition to the minimum voltage level during the fault (V_{nadir}), and the time of its occurrence, t_{nadir}, as they may vary according to the penetration level and according to the technology considered (GFL or GFM), also due to their possible impact on the voltage recovery performance.

4.2.1 | Base Scenario ($p = 0\%$)

Concerning the voltage response at the generation buses when 0% penetration of IBRs is considered, in the base scenario where all generation units are based on SGs only, the deepest voltage dip occurred at bus 1 (0.536 p.u.). In comparison, bus 2 maintained the highest nadir (0.658 p.u.), and bus 3 reached 0.59 p.u., reflecting differences in network strength, coupling to the generation sources, and the relative distance to the fault. All buses have recovered close to unity steady-state voltages (V_{ss} is 1.032, 1.001, and 1.002 p.u., for bus 1, bus 2, and bus 3, respectively. Note that the voltages have recovered with very small deviations (ΔV ≤ 0.024 p.u.) and low overshoot (OS% ranged from 0.987 to 2.445%), confirming well-damped voltage recovery. The voltage nadir occurred almost simultaneously ($t_{nadir} = 0.25$s), indicating a coherent system response. However, Figure 7, shows that bus 1 recovered fastest, reaching 0.9 p.u. at 0.264 s and steady state at 0.535 s, while bus 2 and bus 3 stabilised slightly later (0.637 s and 0.679 s), as shown in Figures 8 and 9, respectively. This shows that bus 1 has a stronger dynamic support due to the closer coupling to the main generation source.

Overall, the zero% penetration scenario demonstrates robust voltage ride-through capability, stable and well-damped voltage recovery, and complete voltage restoration at all generation buses in the system, despite the severe SC fault occurring at the strongest transmission bus in the grid.

4.2.2 | Low and Medium Scenarios ($0\% < p \leq 55\%$)

At low and medium penetration levels (0% < p ≤ 55%), clear deviations from the zero% base scenario appears, reflecting distinct impacts of GFL and GFM IBRs on voltage recovery. For instance, at 22% penetration, the GFL case shows a moderate voltage reduction, with an average Vnadir of 0.485 p.u. across the three buses compared to 0.595 p.u. at zero%. The weakest response occurs at bus 3 (0.3 p.u. vs 0.59 p.u.), as shown in Figure 9, suggesting limited dynamic voltage support from GFL IBRs. The 22% GFM scenario, however, maintains an average V_{nadir} of 0.515 p.u., close to the baseline, which might be due to the fast fault injection and the stronger dynamic voltage support.

At 33% penetration scenarios, the variation in the response of GFL and GFM is clearer. While GFL exhibits an average V_{nadir} of 0.416 p.u., with bus 2 suffering a sharp dip down to 0.149 p.u., marking a major deviation from the 0.658 p.u. at the base scenario (e.g., zero%), GFM RESs maintain an average V_{nadir} of 0.516 p.u., showing improved voltage dynamic voltage support. On the other hand, and despite these variances, both types of IBRs have achieved steady-state voltages near to pre-fault voltage

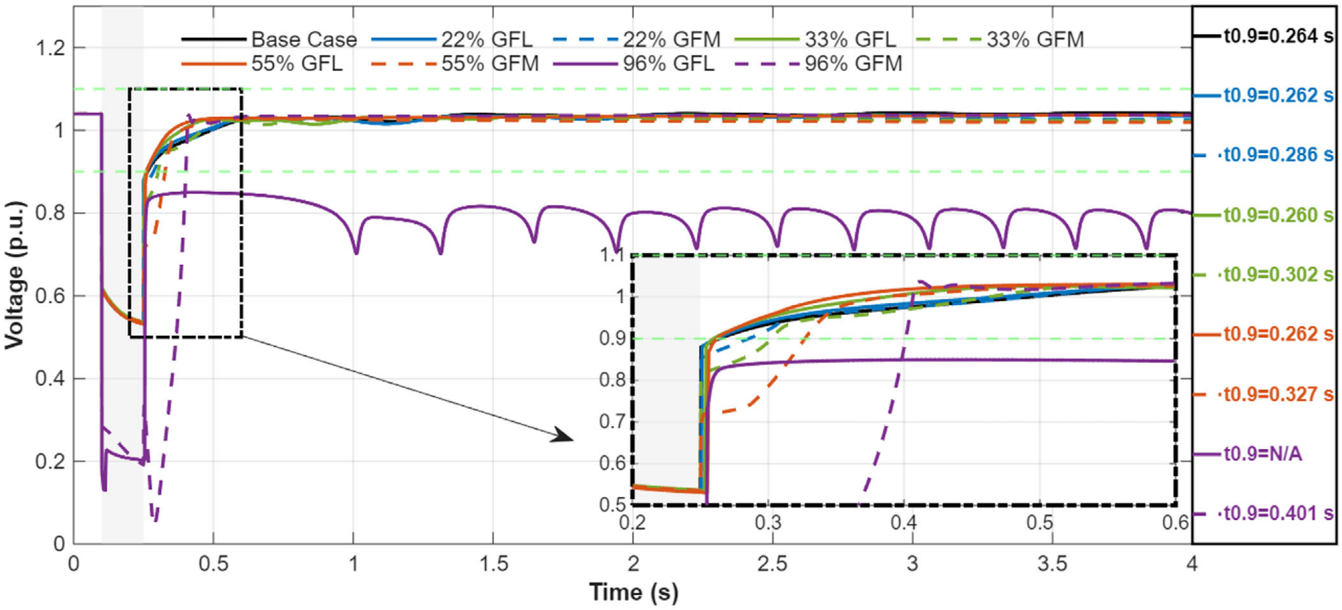

FIGURE 7 | Bus 1 voltage response.

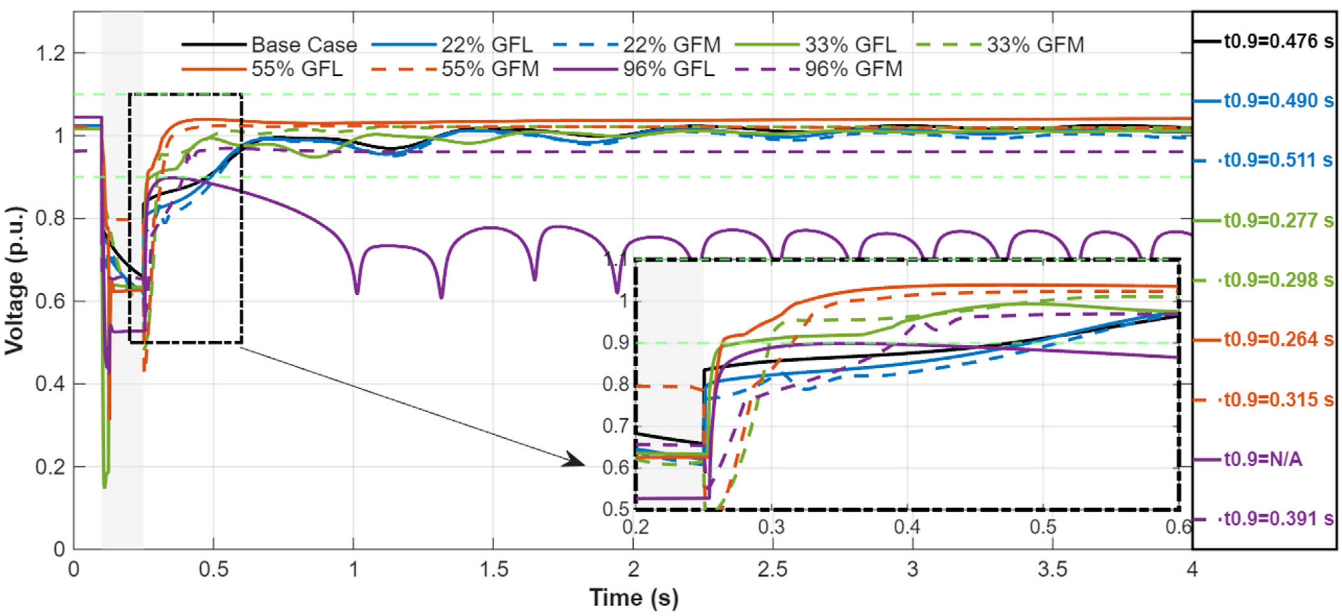

FIGURE 8 | Bus 2 voltage response.

with minor overshoots (OS below 3%). Observe the distinct OS% between GFL and GFM, which is clearer at bus 3 as shown in Figure 9.

At 55% penetration scenarios, average $t_{0\cdot 9}$ and tss are 0.257 s and 0.353 s for GFL versus 0.314 s and 0.364 s for GFM, while Vss is slightly higher for GFL than for GFM. Overshoot remains low (<1%) for both GFL and GFM scenarios, indicating well-damped recovery. However, it can be noticed that the 55% GFM scenario provides more uniform and coherent restoration across all generation buses, supported by Table 3. Observe in this scenario that the steady-state voltages V_{ss} are very close across Bus 1, Bus 2, and Bus 3 (1.020, 1.020 and1.022 p.u.), and the overshoot and ΔV values are minimal, indicating that all generation buses recover consistently and smoothly. This uniformity is a positive outcome because it demonstrates strong dynamic voltage support from the GFM converters and ensures a more predictable and stable system response. Note the Vss of 1.02, 1.02, and 1.022 for buses 1, 2, and 3, respectively, as shown in Table 3; and time metrics of the performance at generation buses are presented in Table 4. Compared with the zero% baseline (average $t_{0.9} = 0.393$ s, $t_{ss} = 0.617$ s, $V_{ss} = 1.011$ p.u), GFL scenarios show slightly faster but less smooth recovery with larger ΔV, whereas GFM scenarios preserve recovery performance closer to

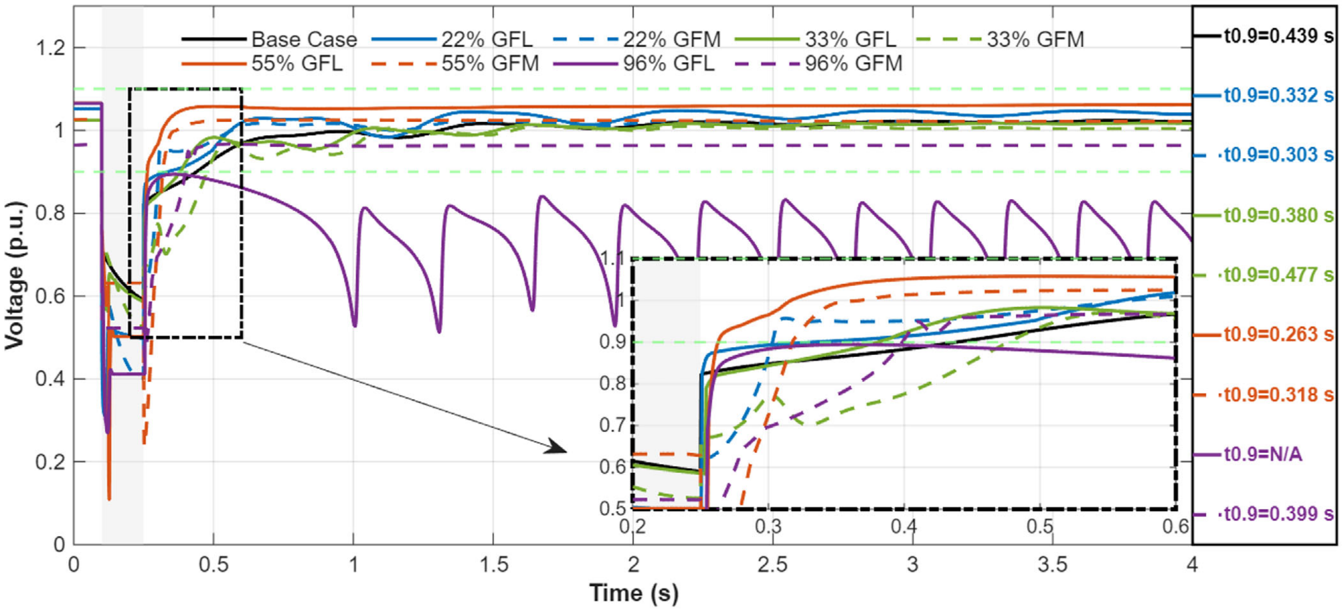

FIGURE 9 | Bus 3 voltage response.

TABLE 3 | Voltage metrics of the response at the generation buses.

Penetration scenario	V_{pre} (p.u)			V_{nadir} (p.u)			V_{ss} (p.u)			ΔV (p.u)			OS (%)		
	Bus1	Bus2	Bus3	Bus1	Bus2	Bus3	Bus1	Bus2	Bus3	Bus1	Bus2	Bus3	Bus1	Bus2	Bus3
Zero%	1.04	1.025	1.025	0.536	0.658	0.59	1.032	1.001	1.002	0.008	0.024	0.023	0.987	2.445	2.209
22% GFL	1.04	1.025	1.052	0.533	0.621	0.3	1.029	0.992	1.026	0.011	0.033	0.026	0.795	2.484	2.095
22% GFM	1.04	1.025	1.025	0.535	0.608	0.402	1.025	0.984	1.013	0.016	0.04	0.012	0.909	2.805	0.949
33% GFL	1.04	1.016	1.025	0.536	0.149	0.562	1.031	0.998	1.000	0.009	0.017	0.025	0.594	1.432	1.821
33% GFM	1.04	1.021	1.025	0.536	0.484	0.527	1.022	1.016	0.985	0.018	0.005	0.041	0.957	0.628	2.697
55% GFL	1.04	1.045	1.066	0.53	0.315	0.109	1.032	1.036	1.057	0.008	0.009	0.009	0.528	0.578	0.569
55% GFM	1.04	1.022	1.026	0.536	0.425	0.236	1.02	1.02	1.022	0.02	0.002	0.004	0.724	0.387	0.341
96% GFL	1.04	1.045	1.065	0.129	0.426	0.269	0.797	0.759	0.754	0.243	0.286	0.312	6.553	18.432	18.665
96% GFM	1.04	0.962	0.965	0.045	0.552	0.452	1.019	0.958	0.958	0.021	0.004	0.007	1.735	1.203	0.967

TABLE 4 | Time metrics of the performance at the generation buses.

Penetration scenario	t_{nadir} (s)			$t_{0.9}$ (s)			t_{ss} (s)		
	Bus1	Bus2	Bus3	Bus1	Bus2	Bus3	Bus1	Bus2	Bus3
Zero%	0.25	0.25	0.25	0.264	0.476	0.439	0.535	0.637	0.679
22% GFL	0.25	0.25	0.12	0.261	0.489	0.332	0.503	0.593	0.57
22% GFM	0.249	0.249	0.241	0.285	0.51	0.302	0.503	0.589	0.544
33% GFL	0.25	0.108	0.121	0.256	0.273	0.377	0.407	0.431	0.476
33% GFM	0.246	0.249	0.244	0.298	0.295	0.473	0.462	0.482	0.528
55% GFL	0.25	0.124	0.123	0.256	0.258	0.257	0.373	0.337	0.35
55% GFM	0.245	0.249	0.249	0.321	0.309	0.312	0.38	0.348	0.365
96% GFL	0.111	0.122	0.117	NaN	NaN	NaN	0.886	0.905	0.869
96% GFM	0.284	0.25	0.25	0.397	0.386	0.394	0.402	0.399	0.402

the baseline. Overall, although they achieve stable voltage recovery, GFL scenarios reduce dynamic voltage support and slightly destabilise voltage recovery at higher penetrations, whereas GFM scenarios maintain strong dynamic response and well-damped, near-nominal voltage restoration, which demonstrates slightly better voltage stability and coherent system performance across all generation buses.

4.2.3 | High Penetration Scenario (*p* = 96%)

At 96% GFL penetration scenario, the system experiences extreme stress across all generation buses. Observe that the voltage dips are very deep (Vnadir average 0.275 p.u., buses 1–3: 0.129, 0.426, 0.269 p.u.), as shown in Figures 7–9, respectively. It is very obvious that the system fails to recover, with Vss remaining below 0.80 p.u., large ΔV, and high overshoot (OS ranged between 6.55%–18.66%), indicating near-collapse.

In contrast, the 96% GFM scenario maintains stronger dynamic support (average Vnadir 0.350 p.u., buses 1–3: 0.045, 0.552, 0.452 p.u.) and near-nominal steady-state voltages (V_{ss} 0.958–1.019 p.u.) with low overshoot (<2%) and coherent recovery around ($t_{0.9}$ = 0.39 s).

Overall, at very high IBR penetration, all generation buses fail to recover voltage under GFL scenarios. In contrast, GFM ensures robust dynamic support and well-damped, near-nominal recovery across all generation buses, highlighting its crucial role in maintaining system stability. Observe both the voltage metrics and the time metrics for a better conclusion.

4.3 | Results at the Load Buses

In order to examine the behaviour of the voltage at the load buses considering different penetration scenarios of GFL and GFM IBRs, the voltage waveforms of the load buses (namely, bus 5, bus 6, bus 8) have been obtained considering the previous severe SC fault at bus 4. Like the previous generation buses, all voltage waveforms and all metrics are obtained, in addition to the minimum voltage level during the fault (V_{nadir}), and the time of its occurrence, t_{nadir}, as they may vary according to the penetration level and according to the technology considered (GFL or GFM), also due to their possible impact on the voltage recovery performance.

4.3.1 | Base Scenario (*p* = 0%)

At zero % penetration, the deepest voltage dip occurs at bus 6 (V_{nadir} = 0.171 p.u.), while bus 8 shows the shallowest dip (Vnadir = 0.507 p.u.), reflecting differences in network impedance and distance from generation. All load buses recover close to unity steady-state voltages (V_{ss} = 0.978, 0.996, 0.997 p.u.) with small deviations (ΔV ≤ 0.023 p.u.) and low overshoot (OS around 2%), confirming well-damped recovery. The nadir occurs almost simultaneously (t_{nadir} = 0.25 s), with average restoration to 0.9 p.u. at $t_{0.9}$ around 0.475 s and full steady state at tss around 0.609 s, slightly slower than generation buses. Compared to generation buses, load buses experience deeper voltage dips and slower recovery, indicating weaker dynamic coupling and the damping effects of network impedance while still achieving stable, well-damped voltage recovery.

4.3.2 | Low and Medium Scenarios (0%<*p*≤55%)

At low-to-medium penetrations, GFL scenarios show progressively deeper dips ($V_{nadir\ average}$ 0.318 p.u. at 55%) and faster initial response (t_{nadir} 0.12–0.25 s), but recovery exhibits slightly higher deviations (ΔV around 0.028 p.u.) and mild overshoot (OS around 0.9%). GFM scenarios maintain higher $V_{nadir\ average}$ of 0.399 p. u., smoother $t_{0.9}$ (0.314 s) and t_{ss} (0.364 s) recovery, and near-nominal steady-state voltages (V_{ss} = 0.987–1.024 p.u.).

Compared to the base scenario, both types of IBRs (GFL and GFM) exhibit slightly slower, less uniform recovery. Compared with generation buses, load buses exhibit deeper dips and slightly delayed restoration, highlighting the combined effects of network impedance and weaker dynamic support. Overall, GFM provides more uniform, coherent recovery across all buses, while GFL, though faster in initial response, shows less stable recovery.

4.3.3 | High Penetration Scenario (*p* = 96%)

At very high penetration, similar to the case when generation buses are considered, GFL scenarios fail to recover voltages at all load buses as shown in Figures 10–12, with Vss ranged between 0.756–0.766 p.u., ΔV between 0.256–0.290 p.u., and high overshoot (OS = 12%–17%), indicating near system collapse; $t_{0 \cdot 9}$ is not achieved. Vnadir values are extremely low, ranged between (0.085–0.291 p.u.), as listed in Tables 5 and 6.

In contrast, 96% GFM scenario maintains a stable voltage recovery, with low overshoot (OS around 1.2%), and coherent recovery ($t_{0.9}$ around 0.399 s, t_{ss} around 0.401 s). Observe that load buses at 96% GFM scenario recover to 0.9 p.u. faster than the zero % scenario, with $t_{0.9}$ around 0.398 s (compared to around 0.475 s at zero %), demonstrating accelerated initial recovery. Steady-state voltages are near nominal (V_{ss} = 0.949–0.966 p.u.) with very small deviations (ΔV = 0.007–0.014 p.u.) and low overshoot (OS around 1.2%). Also, it is worth noting that when comparing load buses recovery to generation buses at 96% GFM, t_{ss} shows effectively identical (approximately 0.401 s), indicating coherent voltage stabilisation across the system, though load buses initially recover slightly slower.

Overall, GFMs at high IBRs penetration scenarios can ensure well-damped, near-nominal, and coherent voltage restoration across all buses. In contrast, GFLs fail to do so, highlighting the crucial role of GFMs in dynamic voltage support and post-fault voltage recovery in weak-grid conditions where SGs are mostly displaced by IBRs.

4.4 | Sensitivity of Voltage Recovery Speed to Fault-Induced Voltage Nadir

This section analyses how the severity of the fault, as represented by the voltage nadir observed during the fault-induced

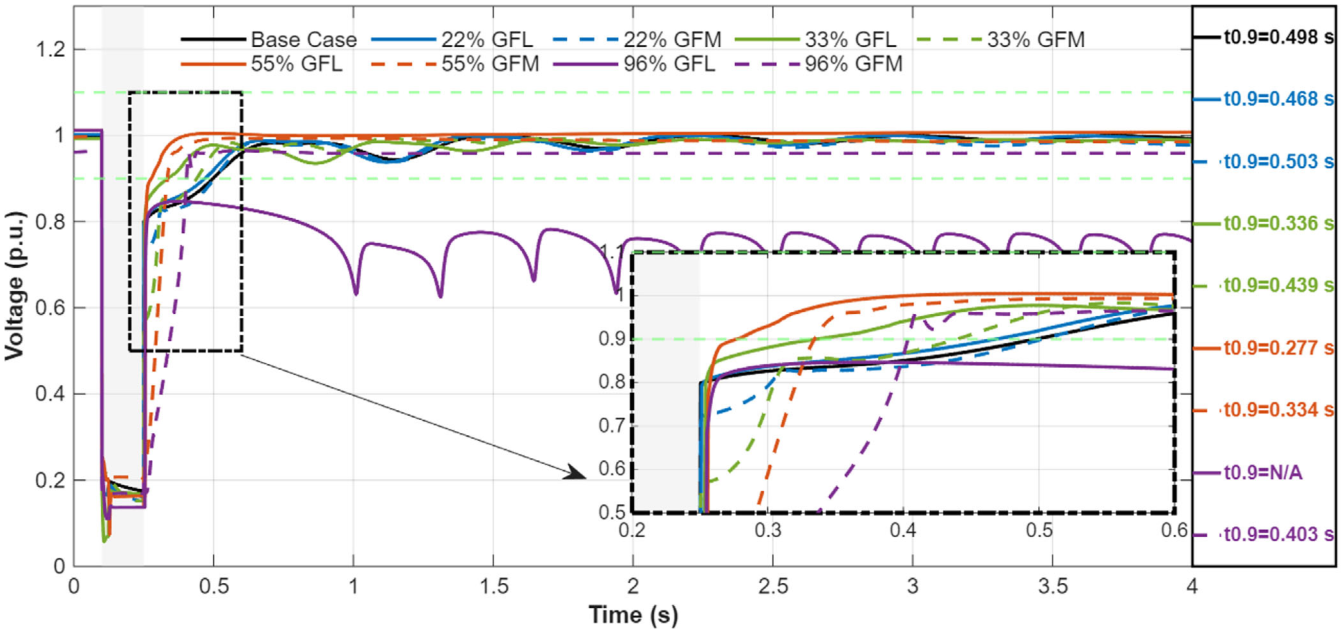

FIGURE 10 | Bus 5 voltage response.

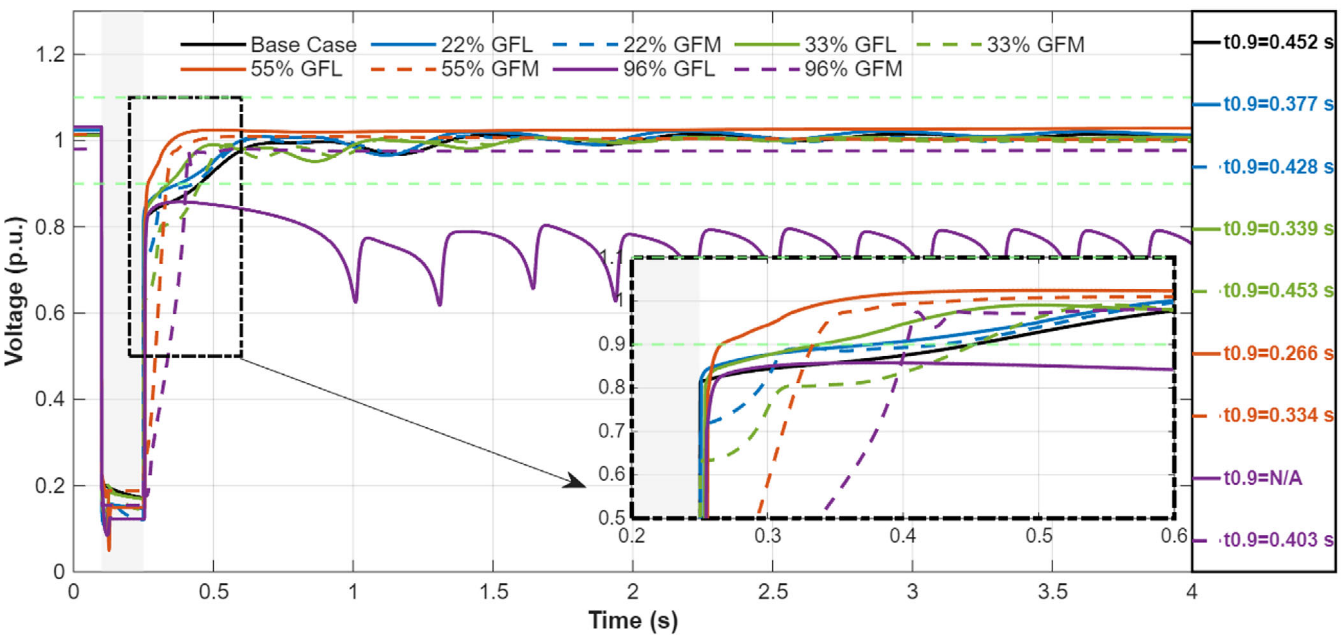

FIGURE 11 | Bus 6 voltage response.

voltage dip, influences the speed of voltage recovery at both generation and load buses under varying levels of IBRs (GFL and GFM). Although these quantities are inherently correlated to some extent, the analysis examines how consistently voltage recovery speed follows fault severity under different IBRs penetration levels and converter types. Note that while the same fault is applied, the resulting voltage nadirs vary across buses and scenarios due to network impedance and dynamic interactions, and the analysis evaluates how this variation translates into recovery behaviour. The significance of this approach lies in assessing whether this coupling remains consistent or changes under different system conditions; in particular, variations in the strength of correlation may indicate shifts in system dynamic behaviour and the influence of converter control strategies.

To assess the effect of fault severity on speed of voltage recovery, the Pearson correlation coefficient (r) between the voltage nadir (V_{nadir}) recorded during the SC fault and the time to 0.9 p.u. recovery ($t_{0\cdot 9}$) was calculated. Distinct analyses were carried out for generation buses, load buses, and all buses together for both

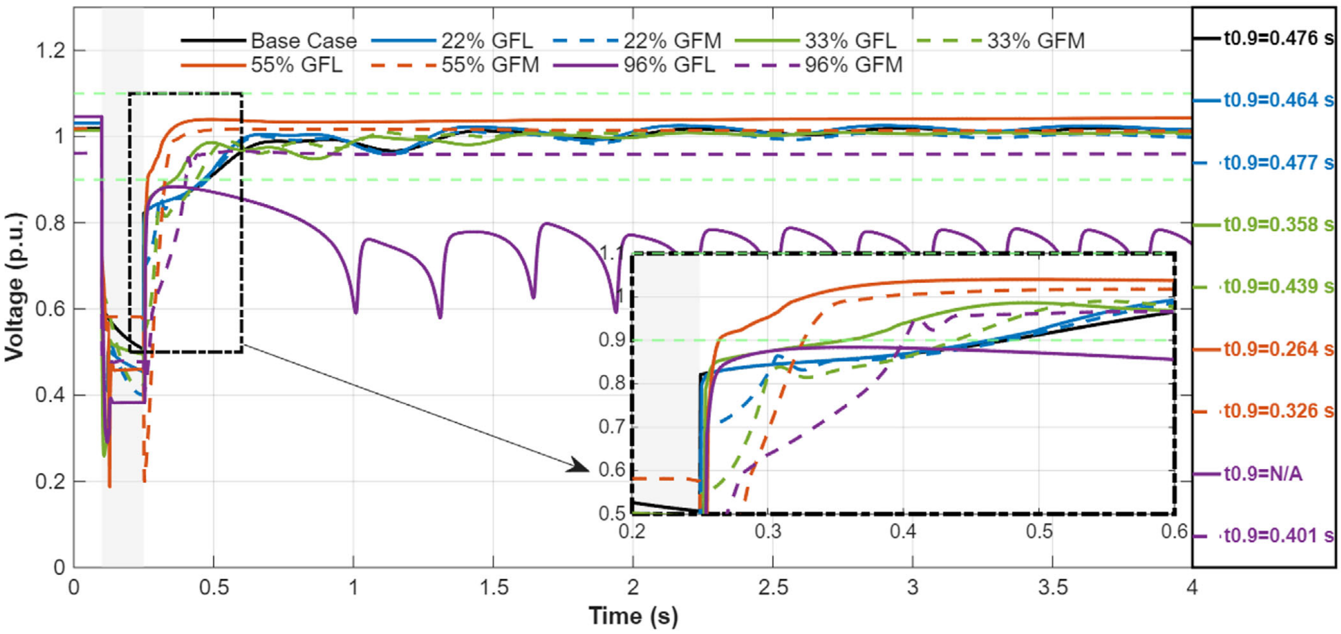

FIGURE 12 | Bus 8 voltage response.

TABLE 5 | Voltage metrics of the response at the load buses.

Penetration scenario	V_{pre} (p.u)			V_{nadir} (p.u)			V_{ss} (p.u)			ΔV (p.u)			OS (%)		
	Bus5	**Bus6**	**Bus8**	**Bus5**	**Bus6**	**Bus8**	**Bus5**	**Bus6**	**Bus8**	**Bus5**	**Bus6**	**Bus8**	**Bus5**	**Bus6**	**Bus8**
Zero%	0.997	1.013	1.019	0.174	0.171	0.507	0.978	0.996	0.997	0.019	0.018	0.023	2.210	1.996	2.355
22% GFL	1.002	1.024	1.031	0.161	0.104	0.410	0.979	1.003	1.002	0.022	0.020	0.029	2.176	1.845	2.350
22% GFM	0.997	1.014	1.019	0.151	0.121	0.400	0.971	0.994	0.990	0.026	0.019	0.029	2.370	1.648	2.150
33% GFL	0.993	1.012	1.015	0.058	0.138	0.260	0.979	0.996	0.995	0.014	0.016	0.020	1.152	1.256	1.538
33% GFM	0.996	1.013	1.018	0.152	0.145	0.420	0.980	0.989	0.996	0.016	0.025	0.022	1.387	1.822	1.629
55% GFL	1.012	1.032	1.047	0.075	0.051	0.187	1.004	1.024	1.038	0.008	0.008	0.009	0.548	0.550	0.572
55% GFM	0.996	1.014	1.018	0.142	0.157	0.200	0.987	1.003	1.013	0.010	0.011	0.005	0.730	0.672	0.447
96% GFL	1.011	1.032	1.047	0.110	0.085	0.291	0.756	0.766	0.757	0.256	0.266	0.290	12.026	11.992	16.743
96% GFM	0.962	0.980	0.961	0.169	0.154	0.407	0.949	0.966	0.954	0.013	0.014	0.007	1.722	1.516	1.242

TABLE 6 | Time metrics of the performance at the load buses.

Penetration scenario	t_{nadir} (s)			$t_{0.9}$ (s)			t_{ss} (s)		
	Bus5	**Bus6**	**Bus8**	**Bus5**	**Bus6**	**Bus8**	**Bus5**	**Bus6**	**Bus8**
Zero%	0.250	0.250	0.250	0.498	0.452	0.476	0.599	0.595	0.632
22% GFL	0.250	0.120	0.120	0.467	0.376	0.463	0.561	0.555	0.576
22% GFM	0.249	0.243	0.249	0.502	0.428	0.476	0.565	0.553	0.571
33% GFL	0.108	0.106	0.107	0.332	0.335	0.354	0.426	0.438	0.444
33% GFM	0.226	0.236	0.228	0.436	0.449	0.435	0.497	0.503	0.506
55% GFL	0.124	0.123	0.124	0.271	0.261	0.258	0.345	0.351	0.346
55% GFM	0.246	0.246	0.249	0.329	0.328	0.321	0.371	0.372	0.360
96% GFL	0.115	0.116	0.116	NaN	NaN	NaN	0.891	0.882	0.887
96% GFM	0.141	0.141	0.250	0.399	0.398	0.396	0.401	0.402	0.401

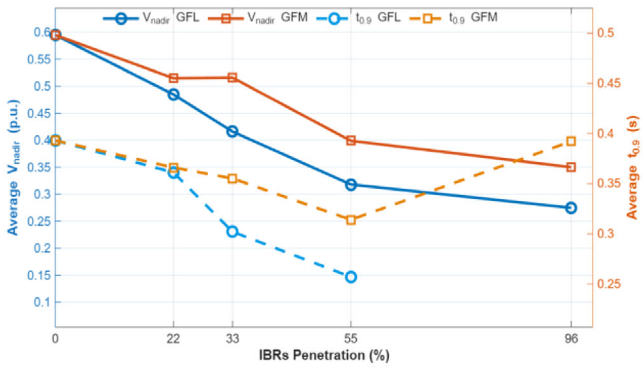

FIGURE 13 | Average V_{nadir} versus average $t_{0.9}$ at the generation buses.

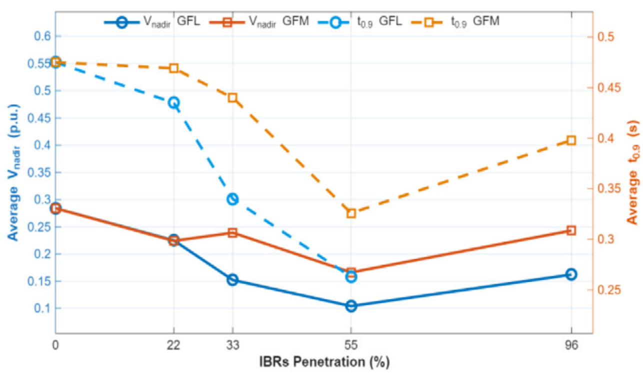

FIGURE 14 | Average V_{nadir} versus average $t_{0.9}$ at the load buses.

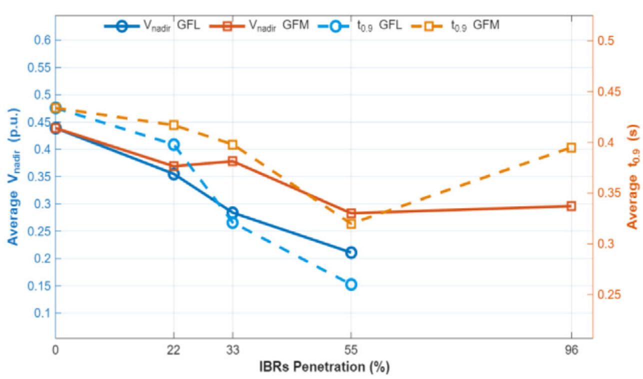

FIGURE 15 | Average V_{nadir} versus average $t_{0.9}$ at all buses.

the GFL and GFM penetration scenarios. It is worth noting that for the scenario in which $t_{0\cdot 9}$ was unavailable (i.e., 96% GFL), these points were excluded from the calculation. This approach allows a numerical evaluation of the sensitivity of the voltage recovery speed to fault severity at different network locations and IBR penetration levels. Note that Figures 13–15 show the average V_{nadir} and the average $t_{0.9}$ of generation buses, load buses, and all buses, respectively. The values of the correlation coefficient (r) for both the GFL and GFM scenarios are listed in Table 7.

For GFL penetration scenarios, the voltage recovery shows a very strong positive correlation with dip depth across all bus types.

TABLE 7 | The correlation coefficient (r) between the (Vnadir) and the ($t_{0\cdot 9}$) at different penetration scenarios.

Penetration scenarios	Bus type	Correlation coefficient (r)	correlation
GFL scenarios	Generation	0.984	Very strong
	Load	0.998	Very strong
	All	0.997	Very strong
GFM scenarios	Generation	0.978	Very strong
	Load	0.925	Strong
	All	0.963	Very strong

At generation buses, r = 0.984, as indicated in Table 7. This is evident from the values of the speed of recovery represented by the averaged $t_{0.9}$ of (0.361 s, 0.302 s, 0.257 s) corresponding to voltage nadirs of (0.485 p.u., 0.416 p.u., 0.318 p.u.) at 22%, 33%, and 55% penetration, as shown in Figure 13. At load buses, r = 0.998, with averaged $t_{0.9}$ of (0.435 s, 0.340 s, 0.263 s) and voltage nadirs of (0.225 p.u., 0.152 p.u., 0.104 p.u.), as shown in Figure 14. Considering all buses combined, r = 0.997, with averaged $t_{0.9}$ of (0.398 s, 0.321 s, 0.260 s) and voltage nadirs of (0.355 p.u., 0.284 p.u., 0.211 p.u.), as shown in Figure 15. These results indicate a highly predictable behaviour as deeper dips consistently trigger faster recovery. Observe a similar conclusion when GFM penetration scenarios are considered. The results show that correlations remain strong, but with slightly more smoothing at load buses. Generation buses show r = 0.978, with $t_{0.9}$ of (0.366 s, 0.355 s, 0.314 s) and voltage nadirs of (0.515 p.u., 0.516 p.u., 0.399 p.u.) at 22%, 33%, and 55% penetration, as observed in Figure 13. Concerning the load buses, it can be shown that they exhibit r = 0.925, with $t_{0.9}$ of (0.469 s, 0.440 s, 0.326 s) and voltage nadirs of (0.224 p.u., 0.239 p.u., 0.166 p.u.), as shown in Figure 14. Finally, across all buses, r = 0.963. Observe Figure 15, where $t_{0.9}$ of (0.417 s, 0.398 s, 0.320 s) and voltage nadirs of (0.369 p.u., 0.378 p.u., 0.283 p.u.), 22%,33%, and 55% GFM penetration scenarios, respectively. These values show that GFM smooths voltage recovery, particularly at load buses, while still maintaining a strong relationship between the recovery speed and the voltage dip during the fault, as characterised by the voltage nadir.

Overall, both GFL and GFM IBRs provide highly predictable voltage recovery across penetration levels. GFL emphasises sensitivity to fault severity, resulting in faster recovery after deeper dips, whereas GFM IBRs moderate recovery at load buses, providing a smoother restoration profile. One more remarkable finding is that, when increasing the IBRs' penetration (GFL or GFM), the voltage recovers faster than in the base scenario (i.e., zero %) when SGs are only in the system.

All in all, the consistently strong correlation between voltage nadir and recovery time highlights the importance of accurately understanding voltage behaviour during faults and the vital role that the FRT control plays in each type of IBRs in speeding the voltage recovery and in achieving a stable and smooth post-fault voltage performance.

5 | Conclusion

A thorough assessment of post-fault voltage response in grids dominated by IBRs was reported in this paper. The effects of IBRs utilising GFL and GFM converters on voltage response during and post-fault under various penetration scenarios are studied.

The findings reveal that when the low and medium penetration scenarios (e.g., up to 55%) are considered at the faulty bus, both GFL and GFM would contribute to fast recovery and low OS% (i.e., <2%), which indicates stable, well-damped voltage recovery. When compared to the base scenario of zero% of IBRs, a faster recovery has been obtained at such low and medium penetration scenarios, with the fastest $t_{0.9}$ observed in GFL scenarios compared to GFM ones, indicating that higher GFL penetration accelerates voltage recovery. On the other hand, when high penetration of IBRs (like 96% scenario) is considered, the results of GFM IBRs have shown an excellent recovery, demonstrating the ability of GFM-based IBRs in contributing to a fast and stable post-fault voltage performance, especially in weak grids with high penetration of IBRs, while GFL-based IBRs suffer to provide a stable recovery after the fault.

At both generation and load buses, low and medium penetration levels of IBRs (up to 55%) result in stable voltage recovery under both GFL and GFM control; however, load buses generally experience deeper voltage dips and slower restoration than generation buses. Scenarios of GFL-based IBRs exhibit faster but less smooth recovery with larger voltage deviations, particularly at generation buses, whereas GFM-based scenarios maintain more coherent and well-damped responses across both bus types, closely resembling synchronous generator behaviour. Under very high penetration (96%), GFL-based systems fail to restore voltage at both generation and load buses, while GFM converters ensure robust dynamic support and near-nominal recovery, underscoring their critical role in stabilising weak, IBR-dominated grids.

One more noteworthy finding is represented by the correlation between the severity of the fault represented by the voltage nadir observed during the fault and the speed of voltage recovery. The correlation analysis shows that for the increased penetration scenarios of IBRs, recovery speed and voltage nadir are strongly correlated. Both IBRs exhibit a strong positive correlation between voltage nadir and recovery speed across all buses (average $r = 0.997$ for GFL, $r = 0.963$ for GFM), providing a predictive insight into post-fault behaviour. Voltage recovery is accelerated when IBRs' penetration is increased in comparison to the SG-only scenario, with GFL recovering slightly faster than GFM. The values of Vnadir are smaller in GFL scenarios compared to GFM, which might be due to the delayed fault injection that leads to higher voltage dip initially; hence, triggering higher dynamic voltage support reactions during the fault, leading to such faster voltage recovery. On the other hand, this might be one of the reasons that lead to instability and missing voltage recovery with high oscillations in weak grids at very high penetrations of IBRs. This suggests that optimised dynamic voltage support and FRT settings are crucial for players, leading to distinct post-fault voltage performance between GFL and GFM IBRs. In addition, it is worth pointing out that extending the study to propose analytical formulations that generalise the correlation analysis is an essential direction for future work.

Collectively, the findings confirm that GFM IBRs can be a promising and practical alternative for substituting the capability of SGs in terms of achieving a stable post-voltage voltage recovery even in weak (i.e., IBR-dominated) grid scenarios. On the other hand, GFL IBRs can still contribute to a stable voltage recovery in relatively strong grids (i.e., mix of SGs and IBRs), but pre-assessment and careful considerations should be taken in mind. Finally, this work identifies some key open research directions, including the impacts of GFM control strategies, current-limiting methods, unbalanced faults, and mixed GFL–GFM operation on post-fault voltage recovery. By highlighting these issues, the study provides a foundation for future research toward reliable IBRs-dominated power systems.

Author Contributions

Rafat Aljarrah: conceptualisation, data curation, formal analysis, methodology, resources, software, visualisation, writing – original draft. **Qusay Salem:** formal analysis, investigation, methodology, resources, software, validation, visualisation, writing – review and editing. **Mazaher Karimi:** funding acquisition, investigation, project administration, supervision, validation, writing – review and editing. **Ibrahim Abuishmais:** conceptualisation, formal analysis, methodology, supervision, validation, writing – original draft. **Hamza Jaber:** data curation, methodology, resources, visualisation, writing – review and editing.

Acknowledgements

Open access publishing facilitated by Vaasan yliopisto, as part of the Wiley - FinELib agreement.

Funding

This work was carried out as a part of the InnoWind project, co-funded by the European Union through the Just Transition Fund (JTF) and administered by the Regional Council of Ostrobothnia (Österbottensförbund).

Conflicts of Interest

The authors declare no conflicts of interest.

Data Availability Statement

No external data has been used for this research.

References

1. ENTSO-E, "Fault Current Contribution from PPMs & HVDC: ENTSO-E Guidance Document for National Implementation for Network Codes on Grid Connection" ENTSO-E, 2017, https://consultations.entsoe.eu/system-development/entso-e-connection-codes-implementation-guidance-d-3/user_uploads/igd-fault-current-contribution.pdf.

2. H. Nguyen, K. Kkuni, T.-L. Nguyen, G. Yang, T.-B. Le, and O. A. Mohammed, "Dynamic Voltage Support Using Fault Current Injection From Converters and Hybrid System," in *2022 IEEE Power & Energy Society General Meeting (PESGM), Denver, CO, USA* (IEEE, 2022), 1–5.

3. R. Aljarrah, B. Fawaz, Q. Salem, M. Karimi, H. Marzooghi, and R. Azizipanah-Abarghooee, "Issues and Challenges of Grid-Following Converters Interfacing Renewable Energy Sources in Low Inertia Systems: A Review," *IEEE Access* 12 (2024): 5534–5561, https://doi.org/10.1109/ACCESS.2024.3349630.

4. R. Aljarrah, M. Karimi, R. Azizipanah-Abarghooee, Q. Salem, and S. Alnaser, "Voltage Dip Propagation in Renewable-Rich Power Systems Utilizing Grid-Forming Converters," *IET Renewable Power Generation* 18, no. 5 (2024): 753–763, https://doi.org/10.1049/rpg2.12939.

5. R. Aljarrah, M. Karimi, H. Marzooghi, et al., "Relationship Between Fault Level and System Strength in Future Renewable-Rich Power Grids," *Applied Sciences* 13, no. 1 (2022): 142, https://doi.org/10.3390/app13010142.

6. W. Sang, W. Guo, S. Dai, C. Tian, S. Yu, and Y. Teng, "Virtual Synchronous Generator, a Comprehensive Overview," *Energies* 15, no. 17 (2022): 6148, https://doi.org/10.3390/en15176148.

7. S. Khan, M. Wang, W. Su, G. Liu, and S. Chaturvedi, "Grid-forming Converters for Stability Issues in Future Power Grids," *Energies* 15, no. 14 (2022): 4937, https://doi.org/10.3390/en15144937.

8. E. Bikdeli, M. Islam, M. Rahman, and K. Muttaqi, "State of the Art of the Techniques for Grid Forming Inverters to Solve the Challenges of Renewable Rich Power Grids," *Energies* 15, no. 5 (2022): 1879, https://doi.org/10.3390/en15051879.

9. B. Bahrani, M. H. Ravanji, B. Kroposki, et al., "Grid-Forming Inverter-Based Resource Research Landscape: Understanding the Key Assets for Renewable-Rich Power Systems," *IEEE Power and Energy Magazine* 22, no. 2 (2024): 18–29, https://doi.org/10.1109/MPE.2023.3343338.

10. J. Beyza and J. M. Yusta, "The Effects of the High Penetration of Renewable Energies on the Reliability and Vulnerability of Interconnected Electric Power Systems," *Reliability Engineering & System Safety* 215 (2021): 107881, https://doi.org/10.1016/j.ress.2021.107881.

11. M. Saleem, S. Saha, U. Izhar, and L. Ang, "Stability Assessment of Inverter-Based Renewable Energy Sources Integrated to Weak Grids," *IET Energy Systems Integration* 6, no. 4: 525–544, https://doi.org/10.1049/esi2.12151.

12. A. Zapata, D. Santos, D. Wu, and D. Rodríguez, "High Penetration of Inverter Based Resources Assessment on Stability and System Strength," in *2023 IEEE Power & Energy Society General Meeting (PESGM), Orlando, FL, USA* (IEEE, 2023), 1–5.

13. S. Shah, P. Koralewicz, V. Gevorgian, H. Liu, and J. Fu, "Impedance Methods for Analyzing Stability Impacts of Inverter-Based Resources: Stability Analysis Tools for Modern Power Systems," *IEEE Electrification Magazine* 9, no. 1: 53–65, https://doi.org/10.1109/MELE.2020.3047166.

14. J. Chow, "Enabling Inverter-Based Resource Stability Control in Power Systems With High Renewable Penetration," *CSEE Journal of Power and Energy Systems* 9, no. 3: 1248–1250.

15. O. Stanojev, U. Markovic, P. Aristidou, and G. Hug, "Improving Stability of Low-Inertia Systems Using Virtual Induction Machine Synchronization for Grid-Following Converters," *IEEE Transactions on Power Systems* 38, no. 3: 2290–2303, https://doi.org/10.1109/TPWRS.2022.3187789.

16. D. Pattabiraman, R. H. Lasseter, and T. M. Jahns, "Comparison of Grid Following and Grid Forming Control for a High Inverter Penetration Power System," in *2018 IEEE Power & Energy Society General Meeting (PESGM), Portland, OR, USA* (IEEE, 2018), 1–5.

17. M. Mirmohammad and S. Azad, "Control and Stability of Grid-Forming Inverters: A Comprehensive Review," *Energies* 17, no. 13 (2024): 3186, https://doi.org/10.3390/en17133186.

18. G. Denis, T. Prevost, M. Debry, F. Xavier, X. Guillaud, and A. Menze, "The Migrate Project: The Challenges of Operating a Transmission Grid With Only Inverter-Based Generation. A Grid-Forming Control Improvement With Transient Current-Limiting Control," *IET Renewable Power Generation* 12, no. 5 (2018): 523–529, https://doi.org/10.1049/iet-rpg.2017.0369.

19. K. Mahmoud, P. Astero, P. Peltoniemi, and M. Lehtonen, "Promising Grid-Forming Vsc Control Schemes Toward Sustainable Power Systems: Comprehensive Review and Perspectives," *IEEE Access* 10 (2022): 130024–130039, https://doi.org/10.1109/ACCESS.2022.3228742.

20. Y. Liu, Y. Wang, X. Liu, M. Wang, Z. Xu, and H. Liu, "Steady-State Angle Stability Analysis of Parallel Grid-Forming Converters in Current Saturation Mode," *IEEE Transactions on Power Electronics* 38, no. 7 (2023): 8039–8044, https://doi.org/10.1109/TPEL.2023.3267624.

21. A. Arjomandi-Nezhad, Y. Guo, B. Pal, and D. Varagnolo, "A Model Predictive Approach for Enhancing Transient Stability of Grid-Forming Converters," *IEEE Transactions on Power Systems* 39, no. 5 (2024): 6675–6688, https://doi.org/10.1109/TPWRS.2024.3368626.

22. H. Xin, C. Liu, X. Chen, Y. Wang, E. Prieto-Araujo, and L. Huang, "How Many Grid-Forming Converters Do We Need? A Perspective From Small Signal Stability and Power Grid Strength," *IEEE Transactions on Power Systems* 40, no. 1 (2025): 623–635, https://doi.org/10.1109/TPWRS.2024.3393877.

23. M. I. Hossain, H. Z. Anonto, A. Shufian, et al., "Enhancing Microgrid Resilience Through Integrated Grid-Forming and Grid-Following Inverter Strategies for Solar PV Battery Control and Fault Ride-Through," *Scientific Reports* 15, no. 1 (2025): 40078, https://doi.org/10.1038/s41598-025-18767-4.

24. J. Rocabert, A. Luna, F. Blaabjerg, and P. Rodríguez, "Control of Power Converters in AC Microgrids," *IEEE Transactions on Power Electronics* 27, no. 11 (2012): 4734–4749, https://doi.org/10.1109/TPEL.2012.2199334.

25. R. Rosso, X. Wang, M. Liserre, X. Lu, and S. Engelken, "Grid-Forming Converters: Control Approaches, Grid-Synchronization, and Future Trends—A Review," *IEEE Open Journal of Industry Applications* 2 (2021): 93–109, https://doi.org/10.1109/OJIA.2021.3074028.

26. V. Babu, J. Roselyn, C. Nithya, and P. Sundaravadivel, "Development of Grid-Forming and Grid-Following Inverter Control in Microgrid Network Ensuring Grid Stability and Frequency Response," *Electronics* 13, no. 10 (2024): 1958, https://doi.org/10.3390/electronics13101958.

27. D. B. Rathnayake, M. Akrami, C. Phurailatpam, et al., "Grid Forming Inverter Modeling, Control, and Applications," *IEEE Access* 9 (2021): 114781–114807, https://doi.org/10.1109/ACCESS.2021.3104617.

28. N. Mohammed, H. Udawatte, W. Zhou, D. Hill, and B. Bahrani, "Grid-Forming Inverters: A Comparative Study of Different Control Strategies in Frequency and Time Domains," *IEEE Open Journal of the Industrial Electronics Society* 5 (2024): 185–214, https://doi.org/10.1109/OJIES.2024.3371985.

29. W. Du, Y. Liu, F. K. Tuffner, R. Huang, and Z. Huang, *Model Specification of Droop-Controlled, Grid-Forming Inverters (GFMDRP_A)* (Pacific Northwest National Laboratory (PNNL), 2021).

30. S. Ganguly, J. Wang, M. Shirazi, and B. Kroposki, "Droop Control-Based Dispatch of an Islanded Microgrid With Multiple Grid-Forming Sources," in *IECON 2023- 49th Annual Conference of the IEEE Industrial Electronics Society, Singapore, Singapore*(IEEE, 2023), 1–6.

31. W. Du, Y. Liu, R. Huang, F. K. Tuffner, J. Xie, and Z. Huang, "Positive-Sequence Phasor Modeling of Droop-Controlled, Grid-Forming Inverters With Fault Current Limiting Function," in *2022 IEEE Power & Energy Society Innovative Smart Grid Technologies Conference (ISGT), New Orleans, LA, USA* (IEEE, 2022), 1–5.

32. B. Weise, "Impact of K-Factor and Active Current Reduction During Fault-Ride-Through of Generating Units Connected via Voltage-Sourced Converters on Power System Stability," *IET Renewable Power Generation* 9, no. 1 (2015): 25–36, https://doi.org/10.1049/iet-rpg.2014.0116.

33. B. Fan, T. Liu, F. Zhao, H. Wu, and X. Wang, "A Review of Current-Limiting Control of Grid-Forming Inverters under Symmetrical Disturbances," *IEEE Open Journal of Power Electronics* 3 (2022): 955–969, https://doi.org/10.1109/OJPEL.2022.3227507.

34. R. Aljarrah, H. Marzooghi, J. Yu, and V. Terzija, "Sensitivity Analysis of Transient Short Circuit Current Response to the Penetration Level of Non-Synchronous Generation," *International Journal of Electrical Power & Energy Systems* 125 (2021): 106556, https://doi.org/10.1016/j.ijepes.2020.106556.

35. N. Baeckeland, D. Chatterjee, M. Lu, B. Johnson, and G. Seo, "Overcurrent Limiting in Grid-Forming Inverters: A Comprehensive Review and Discussion," *IEEE Transactions on Power Electronics* 39, no. 11 (2024): 14493–14517, https://doi.org/10.1109/TPEL.2024.3430316.

36. N. Baeckeland, B. Yang, and G. Seo, "Unified Model of Current-Limiting Grid-Forming Inverters for Large-Signal Analysis," *IEEE Transactions on Power Systems* 41, no. 1 (2026): 198–213, https://doi.org/10.1109/TPWRS.2025.3587224.